Performance review of multiple reference vs. time domain optical coherence tomography

Kai Neuhaus, *Member, IEEE* *, Paul M. McNamara, †, Sergey Alexandrov, Seán O'Gorman,* Josh Hogan,‡ Carol Wilson,‡ Martin J. Leahy.*

* *Tissue Optics and Microcirculation Imaging facility, National University of Ireland, Galway H91 TK33, Ireland.,*
† *Compact Imaging Ireland Ltd., Roselawn House, National Technology Park, Limerick V94 6R68, Ireland.,*
‡ *Compact Imaging, Inc. 897 Independence Ave., Suite 5B, Mountain View, CA 94043 USA.*

DOI: 10.1109/JPHOT.2018.2828419 1943-0655 ©2009 IEEE

This work was supported by NUI Galway, Galway University Foundation, the University of Limerick Foundation, the National Biophotonics Imaging Platform (NBIP) Ireland funded under the Higher Education Authority PRTLI Cycle 4, co-funded by the Irish Government and the European Union - Investing in your future, and Compact Imaging, Inc. All authors have a financial interest in Compact Imaging, Inc. Corresponding author: Martin Leahy (e-mail: martin.leahy@nuigalway.ie).

Abstract: We present a detailed characterization of noise sources in multiple reference optical coherence tomography (MR-OCT) compared to time-domain OCT (TD-OCT). The noise characteristics were modeled based on the TD-OCT noise model and modified for MR-OCT and confirmed with measurements. The MR-OCT sensitivity characteristics are significantly affected by the reflection from the partial mirror, which also introduces a natural attenuation in the reference arm, partially matching the reflectivity intensity profile of human tissue. At optimal balance between sample and reference arm and using balanced detection, the peak sensitivity was measured to be 95 dB, which is close to simple Fourier-domain systems. The results provide a better understanding of the application range for MR-OCT and higher order effects observed, suggesting a non-trivial noise model for MR-OCT.

Index Terms: Heterodyne, Heterodyning, Coherent imaging, Optical coherence tomography, Biophotonics Instrumentation, Coherent imaging

1. Introduction

December 13, 2017

The biomedical optics community is inevitably interested in the advantages of Fourier-domain OCT (FD-OCT) [1], which provides superior noise properties compared to time-domain OCT (TD-OCT). The future of FD-OCT has the potential to be utilized in photonic integrated circuits, promising the smallest ever OCT systems to be developed. Considering the potential of wafer-level FD-OCT, it is easy to overlook that other application-specific technologies can provide valuable complementary functions that require less demanding integration densities and noise parameters. Optomechanical systems used for CD/DVD-ROM pickup-heads, that are currently available, already utilize most of the components that are necessary to create a miniature low coherence interferometric device [2]. The fact that unit costs of these optomechanical systems are as low as 10 USD, suggest that volume production is well understood. Adopting such principles leads to the prospect of developing purpose-built, low-cost TD-OCT systems, which would be

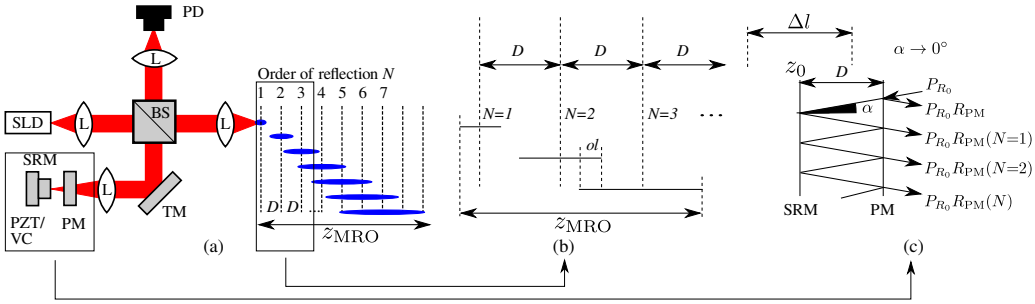

Fig. 1. (a) Schematic of an MR-OCT system. SLD; superluminescent diode, L; lens, BS; beam splitter, TM; turning mirror, PZT/VC; piezo or voice coil actuator, PD; photo detector. The full depth scan is reconstructed from individual orders. The optical path delay is caused by the increased distance of the virtual reflecting layers originating from the multiple reflections between the reference mirror (SRM) and the partial mirror (PM). (b) The increasing scanning range causes overlapping of the scanned layers with an overlapping range ol. The depth location is determined by the optical path delays in the reference arm. (c) The optical path delay is caused by the increased distance of the virtual reflecting layers originating from the multiple reflections between the reference mirror (SRM) and the partial mirror (PM). The geometrical reconstruction of the increasing path delay l is explained by using an exaggerated angle of incident to visualize the path length increase $D(N-1)$. The incidence wavefront from the beamsplitter with a power P_{R_0} is reflected on the PM with reflectivity R_{PM} generating an optical DC with power $P_{R_0} \cdot R_{PM}$. After the wavefront has passed through the PM the power of each further reflection is calculated as $P_{R_0}(1-R_{\mathrm{PM}})^2 R_{\mathrm{PM}}^{(N-1)}$ (N=1,2,...).

assembled with well-understood construction principles. This was the motivation that led to this group's previous work, which investigated the feasibility of enhancing the scanning range of TD-OCT using a partial mirror in the reference arm of a Michelson interferometer [3]. The axial imaging depth z_{MRO} can be calculated based on the relation $z_{\mathrm{MRO}} = \frac{\Delta l}{2}(N+1)+D(N-1)$ using a spacing D between the partial mirror (PM) and scanning reference mirror (SRM), and scanning range Δl. (Fig. 1) [4], [5]. Even by processing only ten optical reflections ($N = 10$ orders), multiple reference OCT (MR-OCT) enhances the axial imaging depth from an otherwise shallow scanning range of 95 µm to 1870 µm using $D = 150\,\mu\mathrm{m}$. The selection of the number of reflections depends solely on the scattering properties of the sample and other optical losses and more than 15 orders have been shown to be useful for imaging.

Understandably, image quality and sensitivity are dependent on multiple other factors that are either simpler for TD-OCT or not required. Due to the more challenging optical noise properties, it is clear that MR-OCT does not try to challenge existing medical grade FD-OCT systems. The strengths of MR-OCT can be found in potential low-cost miniature technologies that are fit for purpose such as simple monitoring tasks. It is undoubtedly not possible to surpass high-end clinical systems in ophthalmology in imaging quality but the resolution and sensitivity are well within range of performing single point measurements of layers in the eye's retina [6]–[8]. For monitoring selected eye related properties in ophthalmology, single shot or small scan range measurements may be sufficient. For such measurements adequate resolution and sensitivity are readily achievable with MR-OCT. This technology can provide valuable support for remote healthcare if used in conjunction with smart-phones, which are currently abundant. Other applications include the improvement of existing biometric databases, which require fingerprint pattern recognition through the addition of liveness detection [9]–[11]. In the area of non-destructive testing, MR-OCT has potential to serve as a surface monitoring system that can include spectroscopic data for each depth point for semi-transparent and scattering materials for a chosen wavelength of light. This has been demonstrated previously using time-domain [12] and spectral domain [13] interferometry. Those applications would benefit from the larger detection bandwidth of the photo-diode compared to charge-coupled detectors in other OCT technologies. [14]–[17].

Another unique feature of MR-OCT is the increasing axial imaging range per order $z_{\Delta \mathrm{l}}(N) =$

$(\Delta l/2)(N+1)$ which causes specific depth regions to be scanned multiple times, since successive orders will eventually (with increasing order) overlap (Fig. 1).

The research efforts for MR-OCT are therefore based on additional properties due to the partial mirror (PM) in the reference arm which are not found in other OCT systems. We compare the step-wise reduction of the powers due to the PM to the reflectance profile of human skin and provide a tentative noise and sensitivity model. This is compared with measurements on a prototype MR-OCT system with a single photodiode and a balanced photo-detection system. The noise model helps to determine the limitations and the application range of MR-OCT.

2. MR-OCT theory

Most of the fundamental theory of MR-OCT is covered by the theory of TD-OCT [18]–[21]. The formation of the interference is the same principle and, in this paper, only the new aspects which are related to MR-OCT are discussed. The relation $I = \rho P$ is used to retrieve the photocurrent at the detector, where the detector responsivity is denoted ρ. The time-dependent power P of the interference for TD-OCT is then described as

$$P = P_r + P_s + 2\sqrt{P_r P_s} G(\Delta l) \cos(\omega t + \phi) \tag{1}$$

where P_r and P_s are the powers in the reference and sample arm. Assuming a light-source with Gaussian spectral characteristics, the function $G(\Delta l)$ is then the Gaussian envelope of the interference spectrum along the pathlength difference between reference and sample arm Δl, the angular frequency $\omega = 2\pi f$, and ϕ the initial phase of the frequency content of the interference [19], [21]. The axial resolution for TD-OCT is commonly defined as the 'round trip' coherence length of the light source:

$$l_c = \frac{2\ln 2}{\pi} \frac{\bar{\lambda}^2}{\Delta\lambda} \tag{2}$$

where $\bar{\lambda}^2$ is the mean of the square of the center wavelength of the light source and $\Delta\lambda$ is the spectral bandwidth at the full-width half-maximum (FWHM) of an assumed Gaussian-shaped spectrum. It should be noted that the round-trip coherence length l_c is half the coherence length of the light source [19], [22]. The superluminescent light emitting diode (SLED) used in this work (DL-CS3152A) has a central wavelength of 1300 nm and a spectral bandwidth of 30 nm, which by (2), gives a best expected axial resolution of 25 µm.

The Gaussian envelope for TD-OCT is given

$$G(\Delta l) = \exp\left[-\left(\frac{2\sqrt{\ln 2}\Delta l}{l_c}\right)^2\right]. \tag{3}$$

For MR-OCT, (3) needs to be extended to accommodate the higher orders of reflections with increasing scanning range. Consequently, we obtain multiple Gaussian envelopes depending on the order N described by

$$G(\Delta l, N) = \exp\left[-\left(\frac{2\sqrt{\ln 2}N\Delta l}{l_c}\right)^2\right]. \tag{4}$$

There is no term in (4) to describe the actual depth layer. That means that during the acquisition time Δt, the interference signal at the detector for all orders of reflections occurs as a summation of the signals. In fact, the true depth location is merely a digital reconstruction after band-pass filtering of the orders based on their Doppler frequency

$$f_D(N) = \frac{2N v_{\mathrm{SRM}}}{\lambda_0}, \tag{5}$$

where v_{SRM} is the linear scanning velocity of the SRM and λ_0 is the center wavelength of the light source. We can describe the apparent scanning range during one acquisition cycle with

$$\Delta l(N)_{\mathrm{digitized}} = (N v_{\mathrm{SRM}})\Delta t \tag{6}$$

indicating the capture of increasing scanning ranges due to increasing SRM velocity into one buffer length and acquisition time Δt. That means during observation of the acquired signal with an oscilloscope, the actual increase of the scanning range represents itself as squeezed signals, e.g. the Gaussian *FWHM* of a mirror signal would reduce to *FWHM*$/N$. Consequently, after band-pass filtering, higher orders need to be upsampled by the factor N to reconstruct the true scanning range.

For the noise discussion we want to evaluate the digitized signal and therefore use (6) to describe the Gaussian shape of the MR-OCT interference signal

$$P_{\mathrm{MRO}} = P_{\mathrm{PM}_0} + \sum_{N\to\infty} \{P_r(N) + P_s(N) + 2\sqrt{P_r(N)P_s(N)}G(\Delta l(N)_{\mathrm{digitized}})\cos(N\omega t)\}. \tag{7}$$

Note that the initial phase term ϕ has been dropped here since the absolute phase is of limited practical use, although the absolute phase will accumulate N more times after reflection from the SRM. It would only be of interest for evaluating the phase difference, which is the same as in TD-OCT.

The power $P_r(N)$ depends on the cumulative reflectivity and can be calculated by summing all orders up to N (Fig. 1). To obtain the reflectivity of reflection N, the equation

$$R_r(N) = R_{\mathrm{PM}} + (1 - R_{\mathrm{PM}})^2 \sum_{N=1}^{N} R_{\mathrm{PM}}^{(N-1)} \tag{8}$$

is used. Not only can (8) be used to confirm that the total reflectivity is unity if all theoretical orders are summed $N \to \infty$, but also to obtain an expression to extract the reflectivity for any order N with (10). The properties of the sequence $R_r(N)$ (8) for reflectivities $N = 1, 2, \ldots$ is geometric [23] and the sum term can be rewritten as

$$S(N) = \sum_{N=1}^{\infty} R_{\mathrm{PM}}^{(N-1)} \tag{9}$$

$$= \frac{1 - R_{\mathrm{PM}}^{(N+1)}}{1 - R_{\mathrm{PM}}} \tag{10}$$

such that for $R_{\mathrm{PM}} < 1.0$ and $N \to \infty$ the sum S becomes

$$S(N \to \infty) = \frac{1}{1 - R_{\mathrm{PM}}}. \tag{11}$$

Substituting (11) into (8) gives

$$R_r(N \to \infty) = R_{\mathrm{PM}} + (1 - R_{\mathrm{PM}})^2 \frac{1}{1 - R_{\mathrm{PM}}} = 1 \tag{12}$$

and the result of unity means that the sum of all reflections from the SRM and the PM describes an ideal mirror again. The power characteristics can now be graphically visualized as in Fig. 2 (solid bold line). Although, not part of this investigation Fig. 2 also shows the characteristics of different splitting ratios of the PM and the power ranges that can be covered vs depth. Fig. 4 shows the power characteristics (Fig. 4).

To some degree, it is possible with MR-OCT to match the power roll-off in the reference arm, relative to the roll-off in a sample (Fig. 5).

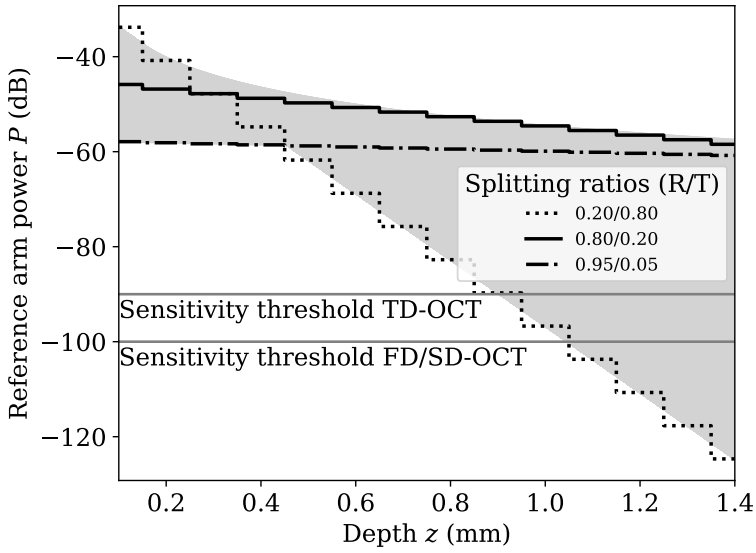

Fig. 2. The reference arm power of MR-OCT was calculated based on the SLED power of 13 mW with a PM splitting ratio of R/T=80/20 (solid bold line) and OD 1.0 attenuation. The gray area represents the possible powers that can be achieved through the selection of other splitting ratios. The boundaries are plotted for ratios R/T=20/80 and 95/5 (dotted and dot-dash respectively). Two guides for assumed sensitivity levels of 100 dB [19] and 90 dB [24] are shown.

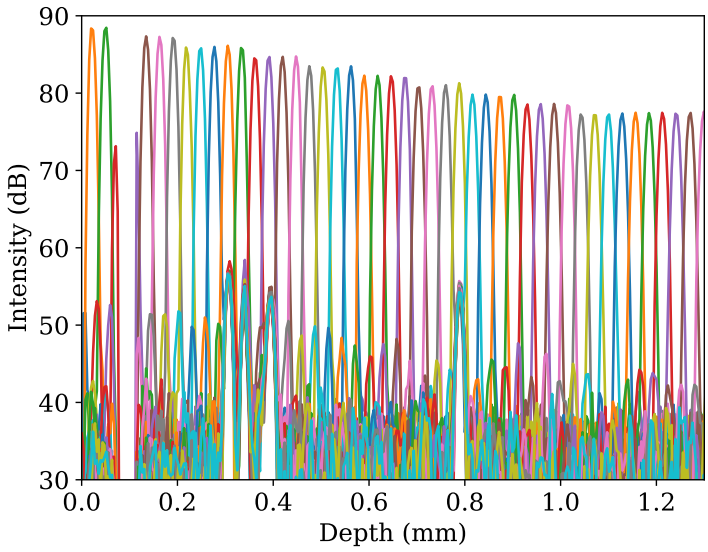

Fig. 3. Multiple point spread functions from a mirror interface are plotted to obtain the intensity profile measured on the maximum peak of the Gaussian shape. The step-like structure is apparent in the peak amplitudes of each Gaussian (which are plotted more clearly in Fig. 4. Because only ten orders were processed, the peaks of the last order level off.

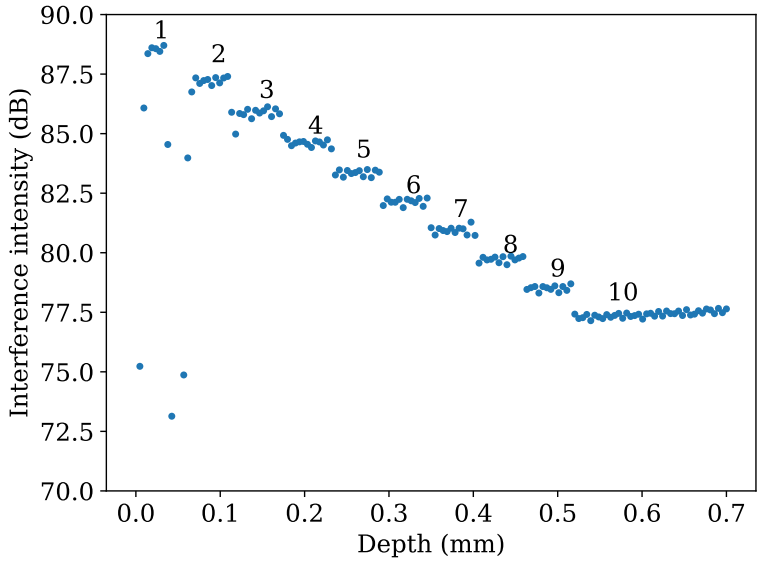

Fig. 4. Distribution of maximum intensities of PSFs taken from Fig. 3. The data points represent ten orders of reflections showing the step pattern for each higher order of reflection. The power at the input aperture of the beam splitter was 13 mW and the refrence arm was attenuated by OD 1.0.

A simplified one-layer tissue model based on Beer's law can be used to predict the power vs. depth [25], [26]

$$I_c(z) = I_L(1 - R_{sp})e^{-\mu 2z} \tag{13}$$

where $I_c(z)$ is the fluence rate at depth z, I_L is the fluence of the incidence beam, R_{sp} the specular reflection coefficient (Fresnel reflection), and μ is the attenuation coefficient ($\mu = \mu_a + \mu_s$) based on the absorption coefficient μ_a and scattering coefficient μ_s. Although the visibility of the OCT signal depends on the refractive index change, the tissue model used here assumes that the attenuation of some ideal reflecting interface is fully described by the value of μ, which accounts for the apparent reflectivity after the light has traveled through the tissue twice by the distance $2z$. The model is hence only valid to calculate the visibility of one reflecting layer at a time, which is fully sufficient to compare the signal vs. depth characteristics with that of MR-OCT (Fig. 4) which is obtained from the maximum peak values from multiple point spread functions from a mirror at different depth positions (Fig. 3).

Fig. 5 shows different signal power roll-offs for different measured μ values of skin tissue. The selected roll-off characteristics are shown as a bold black line. As was already mentioned, in relation to Fig. 4 the slope appears to have a large mismatch, which necessitates the ability to adjust the attenuation for higher orders of reflections (see gray range around the bold line indicating reference arm attenuation from OD 0.0 to OD 4.0). As it is of more interest to capture signals from deeper tissue regions it is better to sacrifice a matching slope and gain the ability to adjust the reference arm power for higher orders of reflections, which is best achieved with a splitting ratio of 0.8/0.2. The mismatch of powers for lower orders of reflections may reduce sensitivity, but due to the stronger signal power, most of the tissue structures will be visible nevertheless. Based on this conceptual understanding, further investigation of different splitting ratios can be discussed, which may become relevant in conjunction with different types of tissue with different attenuation coefficients. The depth range was calculated based on fourteen orders of reflection ($N = 14$) and a PM-to-SRM spacing of 100 µm, resulting in a total imaging depth of 1.4 mm. It is observed that for a splitting ratio of the PM with 0.2/0.8 that the imaging depth is limited by

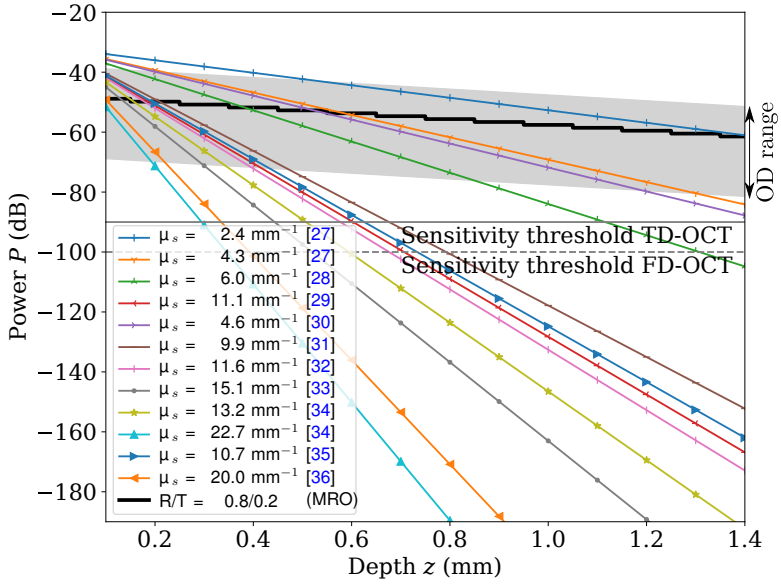

Fig. 5. The power roll-off of dermal structures vs. depth for μ_s values according to various literature resources, calculated with an incident power of 7.5 mW. Sensitivity guides are shown for TD-OCT and FD-OCT [19], [24]. The gray area indicates the range, in which, the MR-OCT reference arm power can be controlled with various attenuations from OD 0.0 to 4.0, and is labeled *OD range*

TABLE I
DETECTOR SIGNALS AND NOISE SOURCES FOR TD-OCT AND MR-OCT

	TD-OCT [19], [24], [37]	MR-OCT
Interference Signal	$\langle I^2_{\mathrm{TD-OCT}}\rangle = 2\rho^2 P_0^2 \gamma_r \gamma_s R_r R_s$	$\langle I^2_{\mathrm{MR-OCT}}(N)\rangle = 2\rho^2 P_0^2 \gamma_r \gamma_s R_r(N) R_s(N)$
DC Signal I_{DC}	$\rho P_0(\gamma_r R_r + \gamma_s R_s)$	$\rho P_0(\gamma_r[R_{\mathrm{PM}} + R_r(\mathrm{N}\rightarrow\infty)] + \gamma_s R_s(N))$
i^2_{shot}	$2q_e\rho P_0(\gamma_r R_r + \gamma_s R_s)B$	$2q_e\rho P_0(\gamma_r[R_{\mathrm{PM}} + R_r] + \gamma_s R_s(N))B$
i^2_{excess}	$\frac{1+\Pi}{\Delta\nu_{\mathrm{eff}}}\rho^2 P_0^2(\gamma_r R_r + \gamma_s R_s)^2 B$	$\frac{1+\Pi}{\Delta\nu_{\mathrm{eff}}}\upsilon_2\rho^2 P_0^2(\gamma_r[R_{\mathrm{PM}} + R_r^{\alpha_2}\mathrm{N}^{\beta_2}] + \gamma_s R_s(N))^2 B$
i^2_{receiver}	$\mathrm{NEC}^2 B$	$\upsilon_1\mathrm{NEC}^2 B$ + $\mathrm{NEC}^2 B(\beta_1 \mathrm{N}^{\alpha_{11}} R_r^{\alpha_1})$

the SNR, although the roll-off is a better match compared to the tissue roll-off (see Fig. 5). The selected splitting ratio of 0.8/0.2 generates a stepwise power reduction in the reference arm that is, although compared to the power reduction slope from the tissue samples much less, sufficient to match a range of data points of power values by tuning the reference arm with an OD filter (shaded area) for optimal sensitivity. Even with a slope mismatch, one can increase the reference arm attenuation to best match it to the power values coming from deeper region of a scattering tissue, while sacrificing some sensitivity of layers close to the surface.

3. Performance of TD-OCT vs MR-OCT

The peak amplitude of the interference signal for TD-OCT [19], [24], [37]–[39] is $I_{\mathrm{peak,SD}} = \rho 2\sqrt{P_r P_s}$, where ρ is the detector responsivity, P_r and P_s are the reference and sample arm

powers, respectively. The responsivity is $\rho = \eta q_e / h\nu_0$ where η is the quantum efficiency of the detector, q_e is the electron charge, h is Planck's constant, and ν_0 is the center frequency of the light source. The model of the sensitivity characteristics uses the equations tabulated in Table I [24]. These are based on the assumption of lossless light propagation in an OCT system. Due to the multiple reference reflections interacting all on the same detector plane it is expected that the equations alone do not account for all the effects. As a result, additional constants were introduced to compensate for any deviations.It was determined experimentally that the equation for excess noise needed to be amplified or attenuated with a factor ν_2, while the impact of the reference reflectivity R_r showed a non-linear characteristic that was modeled by the exponent α_2 and the impact of the order N required an exponent β_2. The reason for these non-linear characteristics is subject to further research but relates most likely to parasitic wave interactions from multiple references and sample reflections. It was generally observed that the receiver noise was smaller than predicted and was hence compensated by a factor ν_1. In addition, the receiver noise expressed non-linear characteristics which were best described with a non-linear effect of the reference arm reflectivity R_r using an exponent α_1, and for the order N a gain factor β_1 and exponent α_{11} achieved the best correlation to measured values.

The power of the superluminescent diode (SLED) is P_0, the degree of polarization is Π, and the effective optical linewidth [19] is $\Delta\nu_{\text{eff}} = 1.5\Delta\nu$ with a full width at half maximum (FWHM) of the Gaussian spectrum $\Delta\nu$. The splitting ratio of the beam splitter of the Michelson interferometer is described [24] by $\gamma_r + \gamma_s = 1$, whereas for this investigation $\gamma_r = \gamma_s = 0.5$ was used. Furthermore, the reflectivity in the reference and sample arm is expressed as $R_r = R_s = 1$, whereas for MR-OCT the reflectivity in the reference arm is $R_{\text{PM}} + R_r(N = \infty) = R_r = 1$, and $R_r(N)$ corresponds to the reflectivity for a particular reflection of order N (see section 2 MR-OCT theory). The model also denotes $R_s(N)$ to indicate that only a fraction of the power depending on the refractive index change contributes to the formation of interference if the waves from the sample and the reference arm are coherent. The value for $R_s(N)$ cannot be measured directly and is encoded in the spectral power of the interference signal, and it depends on the sample structure. As opposed to TD-OCT the shot and excess noise (i^2_{shot}, i^2_{excess}) for MR-OCT depend additionally on DC power from the front reflection of the PM with reflectivity $R_{\text{PM}} = 0.8$. The receiver noise i^2_{receiver} is independent of the reference arm power for TD-OCT. For MR-OCT, the receiver noise becomes dependent on the partial reflections from each other order. That means only one partial reflection at a time is contributing to interference while in this instance all other reflections are merely optical DC. This DC level changes depending on the splitting ratio of the PM and the attenuation in the reference arm resulting in a more complex contribution of the receiver noise. However, the measurements have shown that possibly other higher order effects dictate the receiver noise characteristics, which were modeled using scaling factors, such as υ, α, and β. The scaling factor υ describes a general noise factor, which may compensate any other losses of power or gain not accounted for otherwise. The factor α describes a linear gain or attenuation factor per order and the factor β describes the non-linear impact per order. With all the noise components in place the peak SNR with a single detector (SD) is given as [19]

$$\text{SNR}(N)_{\text{SD}} = \frac{4\rho^2 P_r(N) P_s(N)}{\langle i(N)^2_{\text{sh}} \rangle + \langle i(N)^2_{\text{ex}} \rangle + \langle i(N)^2_{\text{re}} \rangle}, \tag{14}$$

while for balanced detection mode the SNR is twice the SNR of single detection mode [37]. The doubling of the SNR is plausible considering the increase of the signal is squared and the noise increases only by a factor of two.

The sensitivity is defined as the ratio of the reflectivity of a perfect mirror ($R = 1$) to the minimum detectable sample reflectivity ($R_{\text{s,min}}$) i.e. $\Sigma = 1/R_{\text{s,min}}$. Since the sample reflectivity is very much weaker than the reference reflectivity (i.e. $R_s \ll R_r$), the sensitivity can be written as

$$\Sigma(N)_{\text{SD}} = \frac{4\rho^2 P_r(N)}{\langle i(N)^2_{\text{sh}} \rangle + \langle i(N)^2_{\text{ex}} \rangle + \langle i(N)^2_{\text{re}} \rangle}. \tag{15}$$

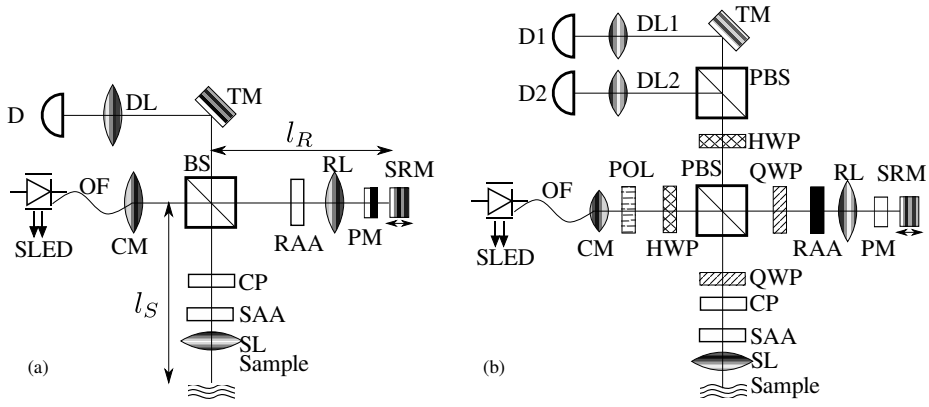

Fig. 6. Two configurations of MR-OCT were used; namely (a) single detection MR-OCT and (b) balanced detection MR-OCT. The components used included SLED: superluminescent diode, OF: optical fiber, CM:collimator lens, BS:non-polarizing beam splitter, PBS: polarizing BS, CP: compensator plate, TM: turning mirror, DL: detector lens, D: detector, SL: sample arm lens, RL: reference arm lens, SRM: reference axially scanning mirror, PM: partial mirror, (S/R)AA: sample / reference arm attenuator, POL: polarizer, HWP: halve wave plate, QWP: quarter wave plate.

It is not practical to attenuate the sample arm completely to obtain SNR=1 but often some attenuation, i.e. provided by an OD = 2 neutral density filter, which provides a roundtrip attenuation of 40 dB and the sensitivity of the system is then the $\mathrm{SNR}_{\mathrm{attenuated}}$ + 40 dB which is often used in literature [19], [24].

4. Optical setup and measurement of sensitivity

4.1. System parameters

For the noise characterization, two different setups were prepared to measure sensitivity with a single detector (Fig. 6a) and with balanced detection (Fig. 6b).

The detectors used were a Throlabs DET10C in conjunction with a trans-impedance amplifier Femto DHPCA-100, and a Newport New Focus 2117 with built-in amplifier. The noise equivalent power (NEP) for the DET10C is specified as 0.025 pW/$\sqrt{\mathrm{Hz}}$ and the New Focus 2117 is 0.4 pW/$\sqrt{\mathrm{Hz}}$ with a responsivity ρ of 0.9 A/W and 1.0 A/W respectively at a wavelength of 1300 nm. Based on the relation $\mathrm{NEC} = \rho\mathrm{NEP}\ [\mathrm{A}/\sqrt{\mathrm{Hz}}]$ the expected NEC values are 0.0225 pA/$\sqrt{\mathrm{Hz}}$ and 0.4 pA/$\sqrt{\mathrm{Hz}}$. The bandwidth is based on the frequency range required for acquisition which was selected with the digitizer of 20 MHz and the receiver noise $\sigma^2_{\mathrm{receiver}} = \mathrm{NEC}^2 B\ [A^2]$ was calculated as 1.01 fA^2 and 0.032 fA^2. Due to the sinusoidal velocity profile of the SRM and zero velocity at the turn-around points the interference signal is chirped, meaning that the Doppler frequency changes from zero to a maximum for each order. The sinusoidal characteristic of the signal is called chirped if the frequency is changing over time and in this particular case the time-dependent change of the frequency is sinusoidal from zero to $N \cdot f_i$ based on the first order interference carrier frequency f_i. The frequency chirp is also directly related to the signal phase which has a sinusoidal characteristic and therefore has non-linear phase.

If the maximum frequency of the 1$^{\mathrm{st}}$ order is 60 kHz, then the fraction of the scanning range with a Doppler frequency below 10 kHz is $[1-\cos^{-1}(10\ \mathrm{kHz}/60\ \mathrm{kHz}\cdot 2-1)/\pi]/2 = 0.134$ or 13% for one side of the scanning range. For a full scanning range with both turnaround points the signal should be limited by 27% to avoid 1/f noise leaking into the signal meaning the useful first order scanning range is 73%. Using the first order limit for all signal orders is a reasonable assumption due to all orders occurring as a sum in the same time-frame.

The quantization noise of the selected digitizer (Picoscope 4824) is determined by the bit width (Q = 12 bit). Using the relation for the quantization SNR (QSNR = $20\log_{10}(2^Q)$) the digitizer would

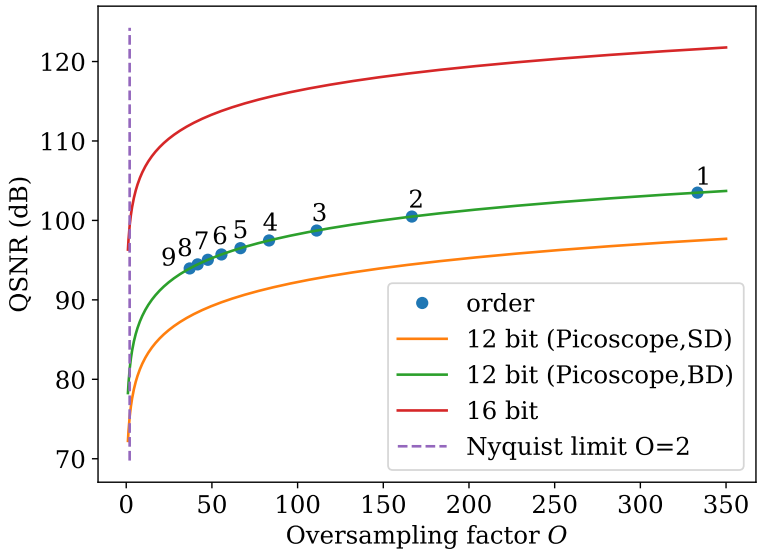

Fig. 7. Digitizer QSNR limitation vs. oversampling factor vs. order of reflection. Due to oversampling the signal SNR can improve somewhat due to averaging effects according to $bit_+ = \log(O)/\log(4)$ where O is the oversampling factor [40]. The position of nine orders of reflections are indicated for the balanced detection limit (12 bit (Picsocope,BD)).

have limited the imaging SNR to 72 dB. With a first order Doppler frequency which was measured on the frequency spectrum with about 60 kHz and a digitizer sampling frequency of 20 MHz, the first three orders were oversampled by more than one hundred times, which theoretically improves the achievable imaging SNR to more than 90 dB for the first five orders of reflection (Fig. 7). This is consistent with the results shown for the sensitivity characteristics.

Fig. 7 confirms that, for systems with expected SNR values above 100 dB, a digitizer with suitable bit-width is essential. It is perhaps not usually of any concern to rely on some advantages by oversampling but it may be interesting to note that for spectral domain OCT (SD-OCT) the oversampling factor is determined by the number of pixels of the line camera vs. frequency components. Any deeper layer will generate a spectral content with higher frequency and advantages gradually diminish. The Nyquist limit for SD-OCT is given as $N_{\mathrm{px}}/2$ [24] based on the number of detector pixels N_{px}.

The frequency spacing between the orders of reflection is determined by their center frequencies $f(N) = Nf$. Consequently the maximum bandwidth for each order is 60 kHz based on the first order frequency. Historically literature discusses the quantisation noise separately to address the conditions of the optical system only. To allow comparison between TD-OCT and MR-OCT the QSNR was therefore not added to the noise model and is considered here as a limiting factor. The discussion of the noise propagation in a digital system until final image formation on the screen is beyond the scope of this paper.

4.2. Sensitivity characteristics for a single detector

Fig. 8 shows the expected sensitivity characteristics for a single detector (DET10C) in TD-OCT. To model the sensitivity for TD-OCT the equations in Table I were used. For TD-OCT no additional fitting parameters were required and the measured values agreed well with the theoretical values (see Fig. 8 solid line). For MR-OCT, additional fitting parameters were necessary, and their values were found empirically, and are listed in Table II. The measured sensitivity for a single detector in TD-OCT follows the model reasonably well, using the fitting parameters $\beta_1 = 0$ ($\alpha_1 = 0$ and

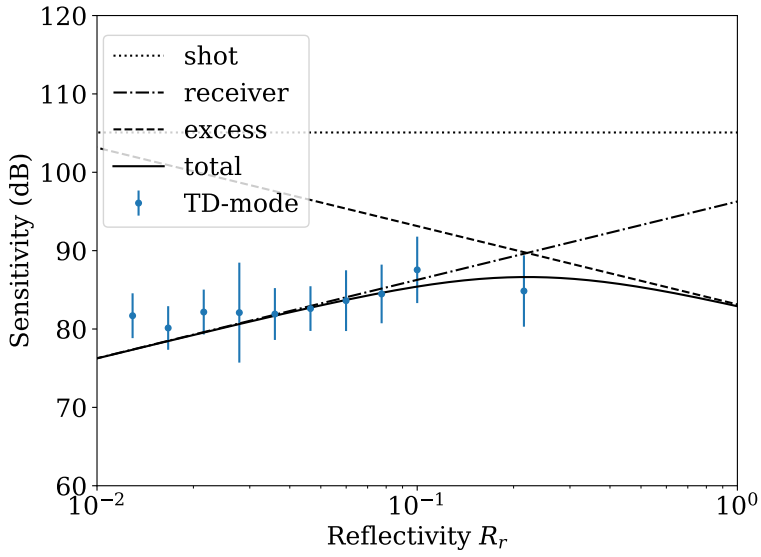

Fig. 8. The measured and modeled sensitivity characteristics for a single detector TD-OCT signal.

$\alpha_{11} = 0$), $\upsilon_1 = 1.5 \times 10^{-2}$, $\alpha_2 = 1.0$, $\beta_2 = 0$, and $\upsilon_2 = 0.0$. The factor υ_1 required some adjustments to account for some power loss to match the expected receiver noise.

Fig. 9 shows the sensitivity characteristics for a single detector MR-OCT system and three orders of reflections (N=2, 6, and 10). For the measurements of sensitivity of MR-OCT, the 1$^{\text{st}}$ order values were neglected due to the limited number of measurements attainable within the 1$^{\text{st}}$ order scan range (i.e. a step size of 25 µm was used and the scan range for the first order was 95 µm). Furthermore, it was not always possible to detect a full point-spread function within the 1st order scan range. Any measured value for the 1$^{\text{st}}$ order sensitivity would be skewed and would not represent the actual achievable sensitivity. In general, the 1$^{\text{st}}$ order is not used for image formation in MR-OCT due to the gap in signal between the 1$^{\text{st}}$ and 2$^{\text{nd}}$ orders. The model parameters used were $\alpha_1 = -1.0$, $\alpha_{11} = 1.8$, $\beta_1 = 8 \times 10^{-3}$, $\upsilon_1 = 1.8 \times 10^{-2}$, $\alpha_2 = 1.4$, $\beta_2 = 0.6$, and $\upsilon_2 = 4.0$.

4.3. Sensitivity characteristics for a dual balanced detector

Fig. 10 shows the sensitivity characteristics of a dual, balanced detector (New Focus 2117) MR-OCT mode. The model parameters used were $\alpha_1 = -1.6$, $\alpha_{11} = 0.7$, $\beta_1 = 3 \times 10^{-2}$, $\upsilon_1 = 5 \times 10^{-1}$, $\alpha_2 = 0.8$, $\beta_2 = 0.5$, and $\upsilon_2 = 3 \times 10^{-2}$. The model does not include effects of the efficiency of the balanced detector, which can reduce the gain advantages as soon as the detectors have slightly different DC offsets. It appears at reference arm reflectivities less than 0.1 that the receiver noise characteristics experience a reduction in slope. The maximum sensitivity of about $R_r = 0.85$ appears to be surpassed for the second order and reaches values close to 100 dB. However, the sensitivity of higher order of reflections is more critical for depth visibility which does not reproduce such sensitivity improvements relative to the maximum peak, meaning that the higher values shown for the second order may more likely relate to increased variance of the measured sensitivity which could be caused due to increasing dominant beat noise [41].

5. Discussion

Table II compares the model parameters used that allow evaluation of contributions of higher order effects for which fundamental principles have not been accounted. The parameters α_1 and α_2

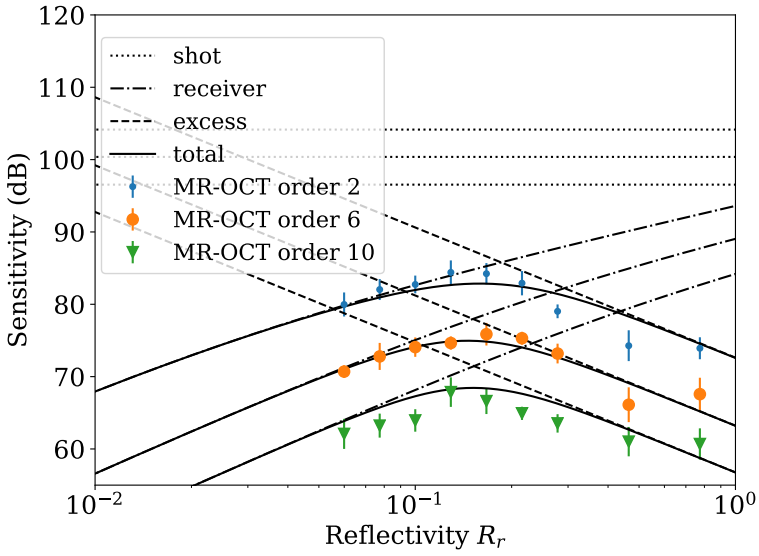

Fig. 9. The measured and modeled sensitivity characteristics for a single detector (DET10C) MR-OCT signal.

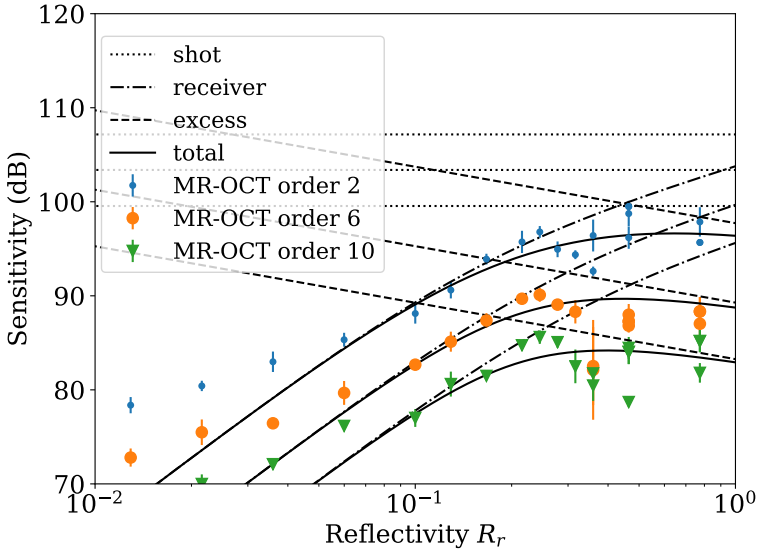

Fig. 10. The measured and modeled sensitivity characteristics for a balanced detector (NF2117) and MR-OCT mode. Please note that the model was weighted towards signal points with larger sensitivity values and does not well account for the characteristics of values close to 80 dB. Also, for $R_r < 0.1$ it can be assumed that the balanced detection provides some gain and the sensitivity rolls off less, while for $R_r > 0.1$ additional noise components exist that are not rejected by the balanced detection and a stronger slope of reduction of the sensitivity can be observed.

TABLE II
COMPARISON OF THE MODEL PARAMETERS

	υ_1	α_1	α_{11}	β_1	υ_2	α_2	β_2
DET10C, TD	0.015	NA	NA	0.0	1.0	1.0	1.0
DET10C, MR	0.018	-1.0	1.8	0.008	4.0	1.4	0.6
NF2117, MR	0.5	-1.6	0.7	0.03	0.03	0.8	0.5

control the exponential power of the reflectivity for a particular order for the receiver and excess noise respectively, and α_{11} controls the exponential power of the linear gain of the reflectivity for the receiver noise per order. The effect of the α-parameters is visually represented in the increased spacing of the sensitivity levels vs order. Another parameter β_1 and β_2 controls the slope of the receiver and excess noise.

For TD-OCT (DET10C, TD) the parameters have no impact or a simple unity relationship confirming the predicted model characteristics of sensitivity. One correction for TD-OCT was required for υ_1, which controls the impact of the receiver noise linearly. The deviation is most likely related to the difficulties in correctly predicting the noise contribution of the combination of detector and amplifier, and depends on bandwidth, gain settings, and the beam power. Nevertheless, even the balanced detector (NF2117) required some reduction of its noise as well. The υ_2 parameter controls a linear correction of the excess noise, which increases for the MR-OCT mode (DET10C, MR). This increase of excess noise could be caused by self-beating of the interference signals from adjacent orders. Interestingly the effect of excess noise with balanced detection (NF2117, BD) is reduced which makes sense if the beat noise can be rejected.

6. Conclusion

The sensitivity characteristics of TD-OCT were confirmed and shown to agree with the model as demonstrated in the literature [19], [24]. A second model for MR-OCT was created and the characteristics of the reference arm power vs. the sample power of different tissue types of human skin were compared. The modeled characteristics showed that tuning the spacing between the partial and scanning reference mirror can provide a variable power balance, which is not available in other OCT systems. Comparing the MR-OCT sensitivity characteristics to the measurements showed that the sensitivity reduces faster vs. the change of the reference arm reflectivity from the optimal balanced condition. The faster sensitivity roll-off may reduce the dynamic range.

Furthermore it was shown that by using a balanced detection method, the sensitivity values for the second order of up to 95 dB or better and for the tenth order more than 85 dB can be achieved. The excess noise was reduced by about two orders of magnitude and the receiver noise by about one order. It was also shown that, for MR-OCT, oversampling could improve the SNR related to the quantization limit and in particular for higher orders it may be significant to choose a digitizer with a larger bit-width.

Other aspects of MR-OCT include the ability to tune or modulate the PM vs. SRM spacing and the potential use of the time-delay of the propagation of each order of reflection at the speed of light. One can compare the spatiotemporal characteristics of overlapping orders that originate from multiple scanned regions within the sample, especially if the PM-SRM spacing is reduced.

References

[1] J. F. de Boer, R. Leitgeb, and M. Wojtkowski, "Twenty-five years of optical coherence tomography: The paradigm shift in sensitivity and speed provided by Fourier domain OCT [Invited]," *Biomedical Optics Express*, vol. 8, pp. 3248–3280, July 2017.

[2] K. Zhang, Q. Zhang, C.-D. Lin, and K.-C. Fan, "A visual non-contact focusing probe for the measurement of micro cavities," *International Journal of Nanomanufacturing*, vol. 11, pp. 207–218, Sept. 2015.

[3] M. Leahy, J. Hogan, C. Wilson, H. Subhash, and R. Dsouza, "Multiple reference optical coherence tomography (MR-OCT) system," in *Proc. SPIE*, vol. 8580, pp. 8580 – 8, SPIE Digital Library, 2013.

[4] R. Dsouza, H. Subhash, K. Neuhaus, J. Hogan, C. Wilson, and M. Leahy, "Voice coil based robust and miniature optical delay for multiple reference optical coherence tomography," Proc. SPIE, pp. 894207–894207–7, International Society for Optics and Photonics, Feb. 2014.

[5] K. Neuhaus, S. O'Gorman, P. M. McNamara, S. A. Alexandrov, J. Hogan, C. Wilson, and M. J. Leahy, "Simultaneous en-face imaging of multiple layers with multiple reference optical coherence tomography," *Journal of Biomedical Optics*, vol. 22, p. 086006, Aug. 2017.

[6] P. Carpineto, M. Nubile, L. Toto, A. Aharrh Gnama, L. Marcucci, L. Mastropasqua, and M. Ciancaglini, "Correlation in foveal thickness measurements between spectral-domain and time-domain optical coherence tomography in normal individuals," *Eye (London, England)*, vol. 24, pp. 251–258, Feb. 2010.

[7] D. J. Browning, M. D. McOwen, R. M. Bowen, and T. L. O'Marah, "Comparison of the clinical diagnosis of diabetic macular edema with diagnosis by optical coherence tomography," *Ophthalmology*, vol. 111, pp. 712–715, Apr. 2004.

[8] C. C. Rosa, J. Rogers, J. Pedro, R. Rosen, and A. Podoleanu, "Multiscan time-domain optical coherence tomography for retina imaging," *Applied Optics*, vol. 46, pp. 1795–1808, Apr. 2007.

[9] A. Zam, R. Dsouza, H. M. Subhash, M.-L. O'Connell, J. Enfield, K. Larin, and M. J. Leahy, "Feasibility of correlation mapping optical coherence tomography (cmOCT) for anti-spoof sub-surface fingerprinting," *Journal of Biophotonics*, vol. 6, pp. 663–667, Sept. 2013.

[10] C. Sousedik and C. Busch, "Presentation attack detection methods for fingerprint recognition systems: A survey," *IET Biometrics*, vol. 3, no. 4, pp. 219–233, 2014.

[11] A. Bossen, R. Lehmann, and C. Meier, "Internal Fingerprint Identification With Optical Coherence Tomography," *IEEE Photonics Technology Letters*, vol. 22, pp. 507–509, Apr. 2010.

[12] M. S. Hrebesh, Y. Watanabe, and M. Sato, "Profilometry with compact single-shot low-coherence time-domain interferometry," *Optics Communications*, vol. 281, pp. 4566–4571, Sept. 2008.

[13] J. Na, H. Y. Choi, E. S. Choi, C. Lee, and B. H. Lee, "Self-referenced spectral interferometry for simultaneous measurements of thickness and refractive index," *Applied Optics*, vol. 48, pp. 2461–2467, May 2009.

[14] V. Jaedicke, S. Ağcaer, S. Goebel, N. C. Gerhardt, H. Welp, and M. R. Hofmann, "Spectroscopic optical coherence tomography with graphics processing unit based analysis of three dimensional data sets," vol. 8592, pp. 859215–859215–7, 2013.

[15] R. N. Graf and A. Wax, "Temporal coherence and time-frequency distributions in spectroscopic optical coherence tomography," *Journal of the Optical Society of America A*, vol. 24, p. 2186, Aug. 2007.

[16] A. Meadway, S. H. H. Darbrazi, R. Cernat, G. Dobre, A. G. Podoleanu, and R. B. Rosen, "Multi-channel time domain spectroscopic optical coherence tomography system," in *Proc. SPIE*, vol. 7139 of *Proc. SPIE*, p. 713909, International Society for Optics and Photonics, Sept. 2008.

[17] A. E. Desjardins, B. J. Vakoc, G. J. Tearney, and B. E. Bouma, "Backscattering spectroscopic contrast with angle-resolved optical coherence tomography," *Optics letters*, vol. 32, pp. 3158–3160, Nov. 2007.

[18] A. F. Fercher, "Optical coherence tomography," *Journal of Biomedical Optics*, vol. 1, no. 2, pp. 157–173, 1996. 00599.

[19] A. Fercher, W. Drexler, C. Hitzenberger, and T. Lasser, "Optical coherence tomography—principles and applications," *Rep. Prog. Phys*, vol. 66, pp. 239–303, 2003.

[20] M. R. Hee, *Optical Coherence Tomography of the Eye*. PhD thesis, Massachusetts Institute of Technology, Dept. of Electrical Engineering and Computer Science, 1997.

[21] M. E. Brezinski, *Optical Coherence Tomography: Principles and Applications*. Academic Press, Aug. 2006.

[22] A. F. Fercher, C. K. Hitzenberger, M. Sticker, R. Zawadzki, B. Karamata, and T. Lasser, "Numerical dispersion compensation for Partial Coherence Interferometry and Optical Coherence Tomography," *Optics Express*, vol. 9, pp. 610–615, Dec. 2001.

[23] I. I. Hirschman, *Infinite Series*. Mineola, New York: Dover Publications, reprint edition ed., Oct. 2014.

[24] R. Leitgeb, C. K. Hitzenberger, and A. F. Fercher, "Performance of fourier domain vs. time domain optical coherence tomography," *Optics Express*, vol. 11, pp. 889–894, Apr. 2003.

[25] S. Ishida and N. Nishizawa, "Quantitative comparison of contrast and imaging depth of ultrahigh-resolution optical coherence tomography images in 800–1700 nm wavelength region," *Biomedical Optics Express*, vol. 3, pp. 282–294, Jan. 2012.

[26] M. J. C. V. Gemert, S. L. Jacques, H. J. C. M. Sterenborg, and W. M. Star, "Skin optics," *IEEE Transactions on Biomedical Engineering*, vol. 36, pp. 1146–1154, Dec. 1989.

[27] U. Sharma, E. W. Chang, and S. H. Yun, "Long-wavelength optical coherence tomography at 1.7 μm for enhanced imaging depth," *Optics express*, vol. 16, pp. 19712–19723, Nov. 2008.

[28] A. R. Knuettel and M. Boehlau-Godau, "Spatially confined and temporally resolved refractive index and scattering evaluation in human skin performed with optical coherence tomography," *Journal of Biomedical Optics*, vol. 5, pp. 83–93, Jan. 2000.

[29] R. R. Anderson and J. A. Parrish, "Optical Properties of Human Skin," in *The Science of Photomedicine*, Photobiology, pp. 147–194, Springer, Boston, MA, 1982.

[30] S. Jacques, "Origins of tissue optical properties in the uva visible and nir regions," *OSA TOPS on Advances in Optical Imaging and Photon Migration*, vol. 2, Jan. 1996. R.R. Alfano and James G. Fujimoto (eds.).

[31] C. R. Simpson, M. Kohl, M. Essenpreis, and M. Cope, "Near-infrared optical properties of ex vivo human skin and subcutaneous tissues measured using the Monte Carlo inversion technique," *Physics in Medicine and Biology*, vol. 43, pp. 2465–2478, Sept. 1998.

[32] I. S. Saidi, S. L. Jacques, and F. K. Tittel, "Mie and Rayleigh modeling of visible-light scattering in neonatal skin," *Applied Optics*, vol. 34, pp. 7410–7418, Nov. 1995.

[33] A. N. Bashkatov, E. A. Genina, and V. V. Tuchin, "Optical properties of skin, subcutaneous, and muscle tissues: A review," *Journal of Innovative Optical Health Sciences*, vol. 04, pp. 9–38, Jan. 2011.

[34] E. Salomatina, B. Jiang, J. Novak, and A. N. Yaroslavsky, "Optical properties of normal and cancerous human skin in the visible and near-infrared spectral range," *Journal of Biomedical Optics*, vol. 11, p. 064026, Dec. 2006.
[35] G. Alexandrakis, F. R. Rannou, and A. F. Chatziioannou, "Tomographic bioluminescence imaging by use of a combined optical-PET (OPET) system: A computer simulation feasibility study," *Physics in medicine and biology*, vol. 50, pp. 4225–4241, Sept. 2005.
[36] S. L. Jacques, "Optical properties of biological tissues: A review," *Physics in Medicine and Biology*, vol. 58, no. 11, p. R37, 2013.
[37] A. M. Rollins and J. A. Izatt, "Optimal interferometer designs for optical coherence tomography," *Optics Letters*, vol. 24, p. 1484, Nov. 1999.
[38] W. V. Sorin and D. M. Baney, "A simple intensity noise reduction technique for optical low-coherence reflectometry," *IEEE Photonics Technology Letters*, vol. 4, pp. 1404–1406, Dec. 1992.
[39] J. F. de Boer, B. Cense, B. H. Park, M. C. Pierce, G. J. Tearney, and B. E. Bouma, "Improved signal-to-noise ratio in spectral-domain compared with time-domain optical coherence tomography," *Optics Letters*, vol. 28, pp. 2067–2069, Nov. 2003.
[40] A. V. Oppenheim, *Discrete-Time Signal Processing*. Upper Saddle River, N.J.: Prentice Hall, 2nd ed. ed., 1999.
[41] H. Hodara, "Statistics of thermal and laser radiation," *Proceedings of the IEEE*, vol. 53, pp. 696–704, July 1965.